Published in final edited form as:
Anal Biochem. 2013 September 1; 440(1): . doi:10.1016/j.ab.2013.05.011.

Improving the Thermal, Radial and Temporal Accuracy of the Analytical Ultracentrifuge through External References

Rodolfo Ghirlando[1], **Andrea Balbo**[2], **Grzegorz Piszczek**[3], **Patrick H. Brown**[2], **Marc S. Lewis**[2], **Chad A. Brautigam**[4], **Peter Schuck**[5,*], and **Huaying Zhao**[5,*]

[1]Laboratory of Molecular Biology, National Institute of Diabetes and Digestive and Kidney Diseases, NIH, Bethesda, MD

[2]Bioengineering and Physical Science Shared Resource, National Institute of Biomedical Imaging and Bioengineering, NIH, Bethesda, MD

[3]Biochemistry and Biophysics Center, National Heart, Lung and Blood Institute, NIH, Bethesda, MD

[4]Department of Biophysics, The University of Texas Southwestern Medical Center, Dallas, TX

[5]Dynamics of Macromolecular Assembly Section, Laboratory of Cellular Imaging and Macromolecular Biophysics, National Institute of Biomedical Imaging and Bioengineering, NIH, Bethesda, MD

Abstract

Sedimentation velocity (SV) is a method based on first-principles that provides a precise hydrodynamic characterization of macromolecules in solution. Due to recent improvements in data analysis, the accuracy of experimental SV data emerges as a limiting factor in its interpretation. Our goal was to unravel the sources of experimental error and develop improved calibration procedures. We implemented the use of a Thermochron iButton® temperature logger to directly measure the temperature of a spinning rotor, and detected deviations that can translate into an error of as much as 10% in the sedimentation coefficient. We further designed a precision mask with equidistant markers to correct for instrumental errors in the radial calibration, which were observed to span a range of 8.6%. The need for an independent time calibration emerged with use of the current data acquisition software (Zhao et al., doi 10.1016/j.ab.2013.02.011) and we now show that smaller but significant time errors of up to 2% also occur with earlier versions. After application of these calibration corrections, the sedimentation coefficients obtained from eleven instruments displayed a significantly reduced standard deviation of ~ 0.7 %. This study demonstrates the need for external calibration procedures and regular control experiments with a sedimentation coefficient standard.

Keywords

sedimentation velocity; sedimentation equilibrium; hydrodynamic modeling

Introduction

Analytical ultracentrifugation (AUC) is a versatile technique used to characterize macromolecules, their interactions and hydrodynamic shapes. Over the past century it has

*direct correspondence to Huaying Zhao or Peter Schuck, National Institutes of Health, Bldg. 13 Rm 3N17, 13 South Drive, Bethesda, MD 20892 zhaoh3@mail.nih.gov or schuckp@mail.nih.gov.

been widely applied to the study of proteins, nucleic acids, polymers and nanoparticles, among others [1–4]. Following significant improvements arising from the digitization of data acquisition and analysis in the second half of the 20th century [5–9], AUC has recently undergone a further transformation, largely due to improved instrumentation in the 1990s [10,11] and, in the last decade, sophisticated data analysis techniques that include global analysis strategies. In particular, the direct boundary fitting of sedimentation velocity (SV) data with Lamm equation solutions [12–15] and explicit size-distribution models [16–18] have greatly enhanced the potential for resolving multiple species in the sample under study, and significantly improved the precision of the analysis. Similarly, efforts to account for experimental details and imperfections, such as the finite acceleration of the rotor [19], the finite time of optical scanning [20], signal offsets from optically unmatched buffer [21], the characteristic noise structure of the SV data [22], time-dependent density gradients from co-sedimenting solvents [23,24], as well as methods to avoid the error-prone graphic pre-determination of the meniscus position [20,25,26] have eliminated many known sources of approximation and systematic errors in previous analyses. Supporting these developments, various detailed step-by-step protocols have been described in order to achieve reproducibility and reduce operator-dependent variations [27–30]. In parallel, advances in the hydrodynamic modeling of macromolecules [31–35] allow for the exploitation of more accurate sedimentation coefficients for the absolute analysis of gross protein conformation or shape based solely on the measured hydrodynamic friction, or the refinement of ensembles of solution structure models from small angle X-ray and/or neutron scattering with the aid of complementary hydrodynamic data [36].

These improvements in AUC data analysis and biophysical modeling bring into focus issues regarding the precision, accuracy and absolute errors of the experimental AUC data, as well as the level of detail that can be reliably interpreted. This is not only pertinent to the research applications mentioned above, chief among them hydrodynamic modeling which routinely requires the highest accuracy, but also in the context of regulatory issues [37–39].

Even though AUC is a first-principle based technique, it does rely on accurate calibration in multiple dimensions, including time, rotor speed, distance from the center of rotation, photometric accuracy and temperature. Each can potentially contribute systematic errors that are not captured even by optimal computational and statistical data analyses. This is highlighted by the very recent discovery of errors of up to 10% in the scan times from current instruments, due to a previously undetected problem with the manufacturer's data acquisition software and/or firmware in use over the past two years [40]. Fortunately, it is possible to independently determine scan times sufficiently well from the modification time-stamp of the data files given by the Windows operating system. Based on this, a correction algorithm was implemented in the program SEDFIT to completely eliminate this issue from further entering the data analysis [40]. Among the other required calibrated measurements, the distance from the center of rotation and the rotor temperature have previously been identified as the most critical and potentially limiting [20,41,42], the latter due to the strong temperature dependence of the aqueous solvent viscosity. In the most recent study on the absolute accuracy of *s*-values that can be determined by SV, Errington & Rowe identified the temperature as a leading instrumental source of systematic errors, and estimated the accuracy of *s*-values to be at best within ± 2-3% [42]. However, they also point out that conducting hydrodynamic modeling in a comparative mode, with multiple samples studied side-by-side in the same rotor and thus exposing them to the identical temperature and radial calibration, one can reliably establish differences in sedimentation coefficients of 0.1% [42]. Such relative sedimentation coefficients have also been found to provide results highly consistent with orthogonal hydrodynamic methods [43], and differences in sedimentation coefficients and boundary shapes have been exploited, for example, for ascertaining ligand-

induced conformational changes of proteins with high sensitivity [44,45]. However, relative measurements are not applicable or satisfactory in many cases.

The objective of the present work is to examine absolute errors in sedimentation coefficients measured by AUC and their variation from instrument to instrument, with the goal of achieving a more consistent and accurate AUC calibration with regard to radius and temperature. For this purpose, we draw on a data set of more than one hundred measurements of *s*-values of a stable standard protein in eleven instruments collected over the course of 18 months, originally conducted to assess data consistency in our laboratories. The immediate motivation to revisit these calibration problems was generated by the measurement of large differences in *s*-values of highly pure EGFP conducted on different instruments and with different optical systems [46], reminiscent of putative, initially unrecognized, or established temperature calibration errors in previous studies by others [41,47-51]. The present work further refines the question of time calibration we have previously communicated [40], and additionally addresses calibrations in temperature and radius.

Accurate temperature calibration is far from trivial, and a number of different methods have been developed over the years. These include devices based on calibrated thermocouples [52–54], infrared radiation [51,55], the melting point of solids [41,48,52], and the use of solutions with temperature-sensitive absorbance properties [49]. Radiometers are now used in the commercial instruments, and routine temperature verification by the manufacturer is performed by a post-centrifugal temperature analysis using a calibrated thermometer. Historically, in the Model E, thermistors were placed at the base of the rotor and electrical contact was established through a needle on the spinning rotor inserted into a stationary mercury pool inside the rotor chamber [51]. Alternative designs for the use of thermistors for suspended rotors without electrical contact used radio-telemetry [53,56]. Along this line, another form of wireless device has more recently become available in the form of the Thermochron iButton® (Maxim Integrated Products, Inc.), which is a small steel-enclosed computer chip that can log NIST-traceable calibrated temperature readings at a resolution of up to 0.0625 °C. It has been applied and validated in a range of scientific applications requiring autonomous temperature measurements (e.g. [57]). In the present work we demonstrate how it can be used in the AUC to measure the temperature of a spinning analytical rotor.

Another critical factor influencing the accuracy of the measured *s*-values in SV, and molar masses in SE, is the radial calibration. This is achieved through optical imaging of reference holes in the counterbalance and, to our knowledge, its accuracy has rarely been critically examined [20]. In order to address this question, we describe the use of a patterned mask that allows for a post-centrifugal correction of radial calibration errors. Finally, we demonstrate that after correction for radius, temperature, and elapsed time, highly consistent *s*-values can be obtained from the entire set of instruments included in the present study. We therefore propose the routine use of these inexpensive and convenient approaches for the external control of critical instrument calibration parameters, along with their verification through control experiments using a standard protein such as bovine serum albumin.

Methods

Temperature Measurements With an iButton® Temperature Logger in a Standard Cell Assembly

Calibrated iButton® temperature loggers DS1922L (Maxim Integrated Products, Inc. San Jose, CA) were purchased from Thermodata (Marblehead, MA). Powered by an on-board battery, they can autonomously measure NIST-traceable temperatures from −10 °C to 65 °C

with an 11-bit temperature resolution, corresponding to increments of 0.0625 °C. A sequence of temperature readings at constant time intervals is stored to on-board memory for later read-out using an adaptor with a USB connection to a computer. Manufacturer provided software was used for programming the data acquisition and for readout.

Their shape, consisting of a circular disk of ~ 17 mm diameter and ~ 6 mm height, and weight of ~ 3 g, makes them suitable for insertion into the aluminum barrel of an AUC cell. In order to achieve good thermal conductance with the rotor and mechanical stability, our in-house machine shop manufactured a holder from a cylindrical block of aluminum alloy having the diameter of an AUC centerpiece. On one side of the holder a cavity was machined to exactly fit the temperature logger, on the other side a pinhole was drilled to facilitate insertion of an external reference thermometer. The holder was grooved on the outside so that it can be aligned along the key-way of a standard cell housing (Figure 1A). The detailed design of the holder for mechanical fabrication is available from the authors on request.

To independently test and calibrate the iButton® we used a NIST certified high-precision thermometer, P795 from ThermoWorks (Lindon, UT), which is accurate to ± 0.015°C (from −50°C to +199.99°C). The probe of this reference thermometer was inserted into the pinhole of the iButton assembly. In order to ensure thorough thermal equilibrium, the iButton®, holder, and reference thermometer probe assembly was inserted into a plastic bag filled with thermal beads and immersed into an ice/water bath (0.0°C) or regulated water bath (Lauda E100) at 21.0 or 30.0°C. After temperature equilibration, based on stable iButton® readings, measurements were made over a period of 10 min. Calibration constants were derived from a linear fit of the manufacturer-calibrated iButton® readings to the reference thermometer readings (Supplementary Figure 1), and applied to all subsequent measurements.

To measure the AUC rotor temperature, the iButton® was inserted into its AUC holder and the whole assembly placed into the rotor. To minimize gravitational stress, the logger was aligned perpendicular to the radius with the battery side facing out. The rotor temperature was set to the desired value (20.0°C) at the centrifuge terminal, the rotor was accelerated to 1,000 rpm and temperature logging, programmed at 2 min intervals, was conducted over the next 2.5 – 3.0 hours. In order to verify the reproducibility of the measurements for all the centrifuges examined, at least two independent temperature measurements were performed with delays ranging from days to months. Furthermore, to systematically test both short-term and long-term variability we selected one centrifuge and conducted multiple measurements within the same day, together with daily measurements over four days.

Measurement of Radial Position and Magnification Using a Mask

To independently measure the radial position, we developed a thin, circular steel mask fabricated from 0.002” stainless steel by electric discharge machining and electroless nickel plating (American Etching & Manufacturing, Pacoima, CA). This is held firmly in place within the AUC cell by sandwiching it between standard windows, and the assembly is held together in the aluminum housing with screw rings pressing onto spacers. The mask was designed to have a rectangular hole in the region of the reference sector, and a sequence of 7 smaller rectangular holes 1 mm wide and 1 mm apart in the region of the sample sector (Figure 1B, C). Machining tolerances were 12 μm, which corresponds to 0.09% of the maximum distance between the features and mask spacings were verified with a Nikon microcomparator. A notch to fit the key-way was designed to help orient and fix the mask (Figure 1C). Once the mask is properly assembled into an AUC cell, its position is fixed and no slippage was detected over months in many runs at 50,000 rpm. During sedimentation velocity experiments, interference or intensity (absorbance) scans of this cell produce a pattern of light and dark that is an image of the mask. As the mask does not have a radial

geometry, the radial scanners will trace a slight diagonal across the millimeter spacing. From this we determine that the recorded spatial period will be 1.0011 mm.

The analysis of the mask image was carried out with a custom-written MATLAB (Natick, MA) program, which will be implemented as a utility function in a forthcoming update of SEDFIT. Multiple scans of the mask were loaded, and apparent positions of the 14 light-to-dark transitions spanning a radius range of 13 mm were determined either by graphically defining a signal threshold, or by determining an average maximum slope in the transition. The resulting apparent radii were plotted against transition number and fit to a linear function to determine the average apparent spacing between the transitions. In this manner, making use of the known true spacing of 1.0011 mm, magnification corrections (and their 68% confidence inter of the radial scanner were determined.

Determination of the Elapsed Time Between Scans

As communicated previously [40], we noticed systematic errors up to 10% recorded for the elapsed centrifugation times in instruments running Version 6.0 (Firmware 5.06) of the ProteomeLab™ XL-A/XL-I Graphical User Interface acquisition software (Beckman Coulter, Indianapolis, IN). As described [40], the file creation or modification time-stamps reported by the computer operating system provide an excellent estimate of the time dilation factor required for correction of these temporal errors. The identification and correction of temporal errors is implemented in both SEDFIT (Version 14.0d and later) and SEDPHAT (Version 10.58 and later).

To compare the true time-intervals between scans with reported time intervals in more detail, the following procedure was implemented for a single SV experiment. Just prior to the start of the experiment, the computer clock was synchronized to a reference clock (Oregon Scientific, Inc., Tualatin, Oregon) reporting US official time. The reference clock is automatically synchronized at least once per day via radio signals from NIST radio station WWVB in Ft. Collins, Colorado. The exact time for the start of rotor rotation was recorded and the absorbance scan time-stamps and time to scan were determined by the onset of audible series of lamp flashes. These measurements for the true time intervals between scans were compared with apparent elapsed times recorded by the Beckman Coulter data acquisition in the header of the data files and with the apparent time differences measured using the computer clock.

Test of Photometric Linearity of the Absorbance System

Another important factor that impacts the accuracy of the sedimentation coefficients derived from SV data is the signal linearity. In order to examine this factor, we utilized an XLA photometric check solution kit (Beckman Coulter, part #338009) consisting of three KNO3 solutions with absorbance values of 0.2, 0.6, and 1.0 at 302 nm in a 12 mm path length cell. We loaded these solutions into cell assemblies with 12 mm Epon charcoal centerpieces and sapphire windows, and collected ten radial absorbance scans at 302 nm and 3,000 rpm. Measured absorbance values were based on averages of these ten scans at radii of 6.0 to 7.2 cm. Prior to and following these measurements, UV-Vis spectra were collected using a Cary 300 Bio UV-Visible spectrophotometer.

Sedimentation Velocity Experiments Using BSA as a Reference Protein

A sample of bovine serum albumin (BSA) was prepared by reconstituting lyophilized powder (catalog #7030, Sigma-Aldrich, St. Louis, MO) in phosphate buffered saline (PBS) to a stock concentration of 10 mg/ml. Samples for SV were prepared by dilution in PBS to a final concentration of 0.5 mg/ml. 400 μl of the solution was loaded into 12 mm Epon charcoal centerpiece AUC cells, using the matching PBS buffer as reference solution. In

each experimental series, the same cells filled with BSA were run in all the analytical ultracentrifuges (Beckman Coulter, Indianapolis, IN). After each run, the BSA was resuspended by gently rotating the cells. Consequently, further experiments on the same sample could be conducted without disassembly and re-loading, thus ensuring an unchanged meniscus position.

An initial series of experiments (study I) was carried out using the same set of three cells each loaded with the same BSA preparation, counterbalance and four-hole rotor. These samples were run in an identical configuration sequentially in eight analytical ultracentrifuges, by the same operator. For each instrument, a radial calibration was performed at a rotor speed of 3,000 rpm prior to the run. The instrument was then stopped, the BSA remixed, the cells re-aligned, and the sedimentation experiment was started following standard protocols [27,28]. Briefly, the rotor was temperature equilibrated at 0 rpm under vacuum for at least 1 hour after nominal agreement between the measured temperature and temperature set-point of 20.0°C. The rotor was then accelerated to 50,000 rpm, and single scan absorbance data at 260 nm or 280 nm were acquired in continuous mode with a step-size of 0.003 cm and time intervals of 3 – 5 min. In centrifuges equipped with Rayleigh optics, interference data were also acquired. The experiment was stopped once the trailing edge of the boundary disappeared from the imaged radial window.

A second set of experiments was carried out (study II) in which the exact rotor temperature was determined at 1,000 rpm using the iButton® assembly prior to the sedimentation velocity experiment of BSA sample. In each run a BSA sample was studied together with the radial mask cell assembly, using the same experimental parameters as in study I. Absorbance data were collected in intensity mode and both the BSA and the mask cell assemblies were identical for each experiment. It is important to note that these cells were not disassembled between runs.

Experimental sedimentation profiles of BSA in solution were analyzed with the program SEDFIT (Version 13.1 and later; sedfitsedphat.nibib.nih.gov) using the sedimentation coefficient distribution $c(s)$ model [16], with a resolution of 200 s-values between 0 and 15 S. The quality of the data fit was evaluated by the root mean square deviation and visual inspection of the residual bitmaps. As the BSA solution contained multiple oligomeric species, the $c(s)$ distributions yielded multiple baseline-separated peaks with a dominant species at 4 - 5 S representing the BSA monomer. The s-value of the monomer was integrated to determine its weighted-average value, and used for comparison. The s-values were not converted to standard conditions of water, and for the purposes of the $c(s)$ analysis the partial-specific volume was set to 0.73 ml/g, the buffer density was set to 1.000 g/ml and the buffer viscosity to 0.01002 cp. Viscosity corrections factors for measured s-values, based on the experimental temperatures, were determined with SEDNTERP (sednterp.unh.edu). Two-dimensional projections of the error surfaces were generated with SEDPHAT, and data were plotted with the software GUSSI (http://biophysics.swmed.edu/software.html).

Application of time stamp, temperature, radial magnification, and scan velocity errors to the data analysis

The Lamm equation [58] governs the ideal sedimentation and diffusion of a non-interacting particle with sedimentation coefficient s and diffusion coefficient D in the centrifugal field:

$$\frac{\partial c}{\partial t}=\frac{1}{r}\frac{\partial}{\partial r}\left[r\left(-s\omega^2 rc+D\frac{\partial c}{\partial r}\right)\right] \quad \text{(Eq. 1)}$$

where $c(r,t)$ is the particle concentration as a function of distance from the center of rotation r and time t, ω denotes the rotor angular velocity, and $s\omega^2rc$ and $D(\partial c/\partial r)$ are sedimentation and diffusion fluxes, respectively. If time is recorded erroneously as t' with a dilation factor τ such that $t = \tau t'$, we obtain a Lamm equation on this time-scale:

$$\begin{array}{c}\frac{\partial c}{\partial t'}=\frac{\partial c}{\partial t/\tau}=\frac{1}{r}\frac{\partial}{\partial r}\left(-\tau sc\omega^2r^2+\tau Dr\frac{\partial c}{\partial r}\right)\\ \frac{\partial c}{\partial t'}=\frac{1}{r}\frac{\partial}{\partial r}\left(-s'c\omega^2r^2+D'r\frac{\partial c}{\partial r}\right)\end{array} \quad \text{(Eq. 2)}$$

with apparent sedimentation and diffusion coefficients s' and D', respectively, that follow:

$$s=s'\times\frac{1}{\tau},D=D'\times\frac{1}{\tau} \quad \text{(Eq. 3)}$$

thus leaving molar mass values determined from s' and D' invariant.

Similarly, if the radius is measured with a translation error Δ and magnification error δ such that $r' = r_0 + \Delta + (1 + \delta)(r - r_0)$, then on this radius scale the Lamm equation becomes:

$$\frac{\partial c}{\partial t}=\frac{1}{r}\frac{\partial}{\partial r'}\left(-(1+\delta)sc\omega^2r^2+(1+\delta)^2Dr\frac{\partial c}{\partial r'}\right) \quad \text{(Eq. 4)}$$

and, with the approximation $\delta\Delta\approx 0$ and a Taylor series of $(1+\delta)^{-1}\approx 1-\delta$,

$$\frac{\partial c}{\partial t}\approx\frac{1}{r'-\Delta+\delta(r_0-r')}\frac{\partial}{\partial r'}\left(-(1+\delta)sc\omega^2\left[r'-\Delta+\delta(r_0-r')\right]^2+(1+\delta)^2D\left[r'-\Delta+\delta(r_0-r')\right]\frac{\partial c}{\partial r'}\right) \quad \text{(Eq. 5)}$$

which at an r_0 in the middle of the cell and negligible translation error becomes:

$$\frac{\partial c}{\partial t}\approx\frac{1}{r'}\frac{\partial}{\partial r'}\left(-s''c\omega^2r'^2+D''r'\frac{\partial c}{\partial r'}\right) \quad \text{(Eq. 6)}$$

The apparent sedimentation and diffusion coefficients s'' and D'' then relate to the true values as:

$$s=s''\times\frac{1}{1+\delta},D=D''\times\left(\frac{1}{1+\delta}\right)^2 \quad \text{(Eq. 7)}$$

which implies a transformation factor for the apparent molar masses ($M\sim s/D$) of $M = (1 + \delta)\, M''$.

The temperature correction simply follows the conventional temperature normalization to standard conditions:

$$s_{20}=s_t\times\frac{\eta_t}{\eta_{20}}\times\frac{1-\overline{\nu}_{20}\rho_{20}}{1-\overline{\nu}_t\rho_t},D_{20}=D_t\times\frac{\eta_t}{\eta_{20}} \quad \text{(Eq. 8)}$$

Since the temperature values were close to 20 °C, contributions from the temperature dependence of the buoyancy were neglected, which then leaves the derived molar mass values invariant.

Additional small corrections arise from the finite time required for the acquisition of absorbance data which originate at small radii and move to higher radii in approximately 0.003 cm increments. As each radial acquisition point requires a small, but finite time for collection, the further the boundary moves from the meniscus the larger the time delay is before its position is recorded. This delay allows further migration to take place. If during a nominal time-interval Δt the particle moves by $\Delta r = s\omega^2 r\Delta t$, the extra time before detection amounts to $\Delta\Delta t = \Delta r/v_{scan}$, where v_{scan} is the linear velocity of the scanner, such that its migration will appear to be $\Delta^* r = \Delta r + s\omega^2 r\Delta\Delta t$, corresponding to an apparent sedimentation velocity $s^* = (\Delta^* r/\Delta t)/\omega^2 r = s(1 + s\omega^2 r/v_{scan})$. Applying similar considerations to the movement across the whole solution column leads to [20]:

$$\frac{s^*}{s} = \frac{1}{1 - \frac{s\omega^2(b-m)}{\nu_{scan}\log(b/m)}} \quad \text{(Eq. 9)}$$

The standard scan settings outlined in the experimental Method and the previously determined scan velocity of 2.43 cm/min [20], lead to a correction of 0.18% in the sedimentation coefficient of the BSA monomer. Alternatively, scan velocity corrections can be directly applied to the model functions in SEDFIT, such that the Lamm equation solutions are evaluated at different points in time for each radial position [20].

In summary, as long as the calibration corrections are small, it is not necessary to transform the radial or time entries of the raw data and instead the sedimentation coefficients, diffusion coefficients, and molar mass values from the analysis of the boundary spread and migration as reported by the original data can be corrected using Eq. 3, Eq. 7, and Eq. 8. Conversely, modest calibration errors will not be apparent from the quality of fit in the computational data analysis. We note that the correction of raw data for time dilation errors is implemented in SEDFIT and that forthcoming versions will also correct for radial magnification errors.

Result

Reproducibility and Sources of Error in Sedimentation Velocity

An initial series of experiments was designed (study I) for the purposes of internal quality control and to identify possible sources of error. We compared uncorrected sedimentation coefficients, s_{exp}, measured experimentally using eight AUCs located on the Bethesda campus of the National Institutes of Health. All instruments in this study I utilized the ProteomeLab™ XL-A/XL-I Graphical User Interface acquisition software version 6.0 (firmware version 5.06), subsequently shown to generate files with systematically underreported scan times [40]. This was unknown at the time. However, since all experiments were conducted under the same conditions, this does not affect any of the conclusions drawn regarding the statistical precision and analysis of factors contributing to run-to-run variations.

The same preparation of BSA was filled in three cells and, alongside a counterbalance, inserted in a 4-hole rotor. This unchanged arrangement of assembled sample cells, counterbalance and rotor was taken sequentially to all AUCs participating in this study to conduct SV experiments, using our standard protocol and collecting data with all available optical systems. Experiments were performed in duplicate with repeat runs conducted several weeks later using the identical samples, rotor, and counterbalance. The data

obtained, presented in Figures 3 and 4, allow for a number of important conclusions to be drawn.

First of all, the BSA sample is highly stable and provides reproducible results over the time-course of many months. Furthermore, identical s_{exp}-values were obtained (within the error of the method) when the same batch of lyophilized powder was dissolved more than a year later. Undoubtedly the $c(s)$ data analysis method contributes significantly to this reproducibility, since it allows for baseline resolution of the monomer, dimer and higher BSA oligomers typically observed (Figure 2). As the BSA monomer is baseline separated from the higher order species, the s-value of the monomeric species is independent of the slow and irreversible oligomerization processes. We also found that the sample can be completely resuspended following sedimentation, even though it is transiently present at very high concentrations at the bottom of the cell. This may be related to the fact that albumin is present naturally at very high concentrations in serum.

Another important feature related to the data analysis is that the meniscus value is refined and not fixed or constrained. As pointed out previously [20], the graphical determination traditionally required for pre-computer analysis methods introduces errors for several reasons [20,59], including the fact that the width of the optical artifact is relatively broad when compared to the precision of the computational determination of this parameter [26]. Although none of the data sets in this study showed any evidence for convection, subtle influences of this factor can be strongly diminished by adding the degree of freedom for the meniscus position to the analysis. This essentially obtains molecular sedimentation velocity information only from the successively measured boundary positions, to which the computational determination of the meniscus position amounts [20]. Figure 3A shows a scatter plot of the calculated best-fit meniscus positions for one cell assembly jointly with the determined best-fit s-values, both of which are physically unchanged in any of the experiments and should therefore be identical. Even though the raw s_{exp}-values scatter within roughly 3%, no correlation can be detected with the best-fit meniscus position, which varied within a 0.020 cm range.

To examine the relationship between meniscus and s_{exp}-values in more detail, sedimentation profiles were simulated (based on the average meniscus and s_{exp}-values), and re-analyzed using fixed impostor meniscus positions. The resulting s_{exp}-values (Figure 3A) are shown by the solid green line, with the vertical grey lines indicating meniscus positions that would already be visually rejected on the basis of the quality of residuals of the fit. The two-dimensional error surface showing parameter cross-correlation is provided in Figure 3B, with the red thin line close to the minimum representing a 95% confidence limit – indicating a statistical error of 0.004 cm in the meniscus position and ~0.045 S in the sedimentation coefficient. The black line in Figure 3B indicates the best-fit s-value at a given meniscus value (corresponding to the green line in Figure 3A). Statistical errors in meniscus assignment are therefore not the dominant factor for data scatter as the experimental data points do not follow the green line.

To probe an alternate scenario, artificial linear calibration errors were introduced that offset all radii and translate the apparent meniscus position. The purple line in Figure 3A depicts the correlation between the calculated apparent shift in the new best-fit meniscus position and the best-fit s-value from an analysis that allows the meniscus position to refine. The fact that the experimental data does not correlate with the purple line either suggests that radial calibration errors could occur that translate the apparent meniscus position without affecting the measured s_{exp}-values. This is consistent with the notion that the errors δr in the absolute radial position of the sample in the centrifugal cell will, to a first approximation, lead to

proportional errors in the centrifugal field $\omega^2\delta r$, therefore to relative errors of $\delta s/s = \delta r/r$, which across the range of the grey lines in Figure 3A would amount to 0.01 S (or ~ 0.2%).

On the other hand, temperature calibration errors within the manufacturer's specification of ± 0.5 °C would translate, *via* the accompanying viscosity change, to errors in the *s*-value of ± 0.07 S, as indicated by the dotted purple lines. It is interesting that most experimental measurements fall within these limits. Thus, we hypothesized that absolute errors in the measurements of radial positions in conjunction with uncorrelated temperature errors would be consistent with the present data. This motivated us to study both of these factors in more detail, as described below.

The full results for all three replicate cells are shown in Figure 4. In this scatter plot of *s*-value *versus* meniscus value, symbols with the same colors indicate the same instrument, with circles depicting absorbance data and squares the interference data. The data clearly demonstrate once again the previously observed fact that s_{exp}-values measured side-by-side in different cells in the same rotor and with the same optical system are highly consistent [42] with a standard deviation of 0.0070 S, or 0.15% for the present data. In addition, with few exceptions, in each of these patterns all symbols are paired with their replicate symbol close by, from which it can be deduced that replicate measurements taken from the same instrument but in a different run (using the same rotor, cell, and optical system) still have an excellent reproducibility with an average standard deviation of 0.0169 S, or 0.36% for the results from all cells and both runs from individual machines. The fact that this is ~ 10-fold smaller than the overall variation of *s*-values suggests that in the run-to-run variability of a single instrument, neither radial calibration nor temperature is a significant factor. In contrast, we can conclude that the dominant errors between instruments arise from instrumental factors relatively constant over the time-course of weeks. For example, these could reside in the specific geometry of the optical imaging system, and/or instrumental temperature measurement/calibration.

In an unrelated study [46], we determined sedimentation coefficients for the GluA2 glutamate receptor amino terminal domain and enhanced green fluorescent protein (EGFP). In a comparison of the s_{exp}-values obtained using an instrument from the above set with those from a separate instrument, we observed large, systematic differences amounting to ~ 10%, as reported in [46]. These deviations prompted us to revisit and repeat our BSA control experiments on the same set of instruments used for study I. Approximately 18 months later, most of the instruments provided very consistent values (Table 1 and Supplementary Table T1). However, we found the values from one single analytical ultracentrifuge to exhibit significant deviations from its previous value, indicating a shift, which we believe to have occurred in an adventitious, discontinuous event. For this reason, we sought to develop devices for the independent control of the radial imaging and temperature accuracy.

Measurement of the Rotor Temperature

To measure the rotor temperature, we considered the application of a miniaturized autonomous temperature logger (iButton®) to AUC and initially tested their mechanical integrity in a centrifugal field. We observed they cannot withstand the high fields at 50,000 rpm at the radius of the rotor holes; fortunately no damage could be discerned at 3,000 rpm and below. Obviously one could greatly reduce these gravitational stresses by centering the chip on the rotor's axis of rotation. However, to arrive at a convenient, inexpensive and reversible method we avoided modifications of the rotor or rotor handle. Therefore, we designed a holder to place the iButton® in the rotor holes and restricted the rotor speed for temperature measurement to 1,000 rpm. The holder is fabricated from aluminum to provide good thermal conductivity with the rotor (Figure 1A).

To check and improve on the manufacturer's calibration, we recalibrated the iButton® in the range of 0 to 30 °C using a NIST certified reference thermometer (Supplemental Figure 1). We also verified that neither the application of vacuum nor the gravitational field up to 700 *g* had any effect on the temperature reading within the accuracy of the device (data not shown). Finally, we conducted a series of replicate experiments over the course of several days in the same AUC using the same set-temperature of 20.0 °C, and found that iButton® readings did not differ by more than the resolution of the device. Replicates measured in some instruments between 11 and 50 days after the initial measurement on the same instrument gave readings consistent with a standard deviation of 0.15 °C. It is important to note that no instrument service or repairs occurred during this time period.

Next, we conducted rotor temperature measurements on a number of ultracentrifuges set to a nominal rotor temperature of 20.0 °C. As is evident from the measured temperature *versus* time that can be retrieved from the logger, thermal equilibrium was established only after 90 min of centrifugation. This thermal equilibration time exceeded the ~ 40 min required for the radiometry-based temperature reading displayed at the AUC terminal to arrive at the set point. The equilibrated rotor temperatures measured with the iButton® for the ten instruments are listed in Table 1. Overall, the temperatures ranged from 17.15 to 21.31 °C, with an average of 19.58 °C and a standard deviation of ± 1.04 °C. Notably, one particular instrument gave a reading of 17.15 °C. If the highest and lowest readings are excluded from the set, the average temperature was 19.69 °C with a standard deviation of ± 0.37 °C, comparable to the manufacturer specifications of ± 0.5 °C. Using the complete data set, the maximum difference of ~ 4 °C will lead, based on the steep temperature-dependence of the viscosity of water, to a 10.4% variation in the *s*-value.

Systematic SV experiments with BSA were carried out immediately following the temperature measurements (study II), resulting in experimental s_{exp}-values listed in the third column of Table 1. We have previously documented large errors in the reported scan times [40] and denote *s*-values already corrected for scan time problems by a subscript τ. By including multiple replicates with different optical systems and different wavelengths, the average $s_{exp,\tau}$-value was determined to be 4.192 S with a standard deviation of ± 0.138 S (3.29%) (Table 1, column 9; Figure 6, green stars and Figure 7, s-t). Not surprisingly, the instrument with the lowest temperature gave the lowest s_{τ}-value, although the instrument with the highest temperature did not exhibit the highest s_{τ}-value due to compensating radial magnification errors, as described below. Based on the measured temperatures we calculated a viscosity correction factor to convert the experimental s_{exp}-values to actual $s20$-values (Table 1, column 5), resulting in an average temperature and time corrected $s_{20,\tau}$-value of 4.267 S with a reduced standard deviation of ± 0.083 S (1.95%).

Prior to this study II, we were unaware of the grossly incorrect temperature calibration in the specific instrument having the largest temperature error. It is reasonable to ask whether deviations of 1 -3 °C are rare, and whether ignoring such large calibration errors the *s*-values would still show improvement. Excluding data from the two instruments with temperatures of 17.2 and 21.3 °C, the average $s_{exp,\tau}$-value prior to correction exhibited a standard deviation of ± 0.66 S; after correction the standard deviation was distinctly improved at 0.49 S, reducing the relative error from 1.5% to 1.1%.

Additional opportunities for analysis arise as the BSA solution was reconstituted from the same lyophilized powder in both studies I and II, and many of the instruments were the same in both studies. It is noteworthy that, with the exception of the two instruments with the largest temperature difference, all instruments showed s_{exp}-values with remarkably little change. The average difference of *s*-values from individual instruments in study I and study II was 0.027 S or 0.57% and the overall average s_{exp}-value was 4.707 S in study I and 4.671

S in study II, the latter 0.77% higher. The fact that these variations are smaller than the overall variation of 1.5% further demonstrates that the dominant factors are instrument specific factors, which are stable over the long term. Exceptions are the two instruments that experienced catastrophic changes in its temperature calibration. After conducting study II, we measured the temperature in the instrument with the largest error over several months, and did not observe any drift. We believe, therefore, that a sudden and inexplicable shift occurred at one time after study I and prior to study II. Further, as the reproducibility in individual instruments is better than the time- and temperature-corrected *s*-values suggests the presence of additional factors.

Measurement of the Elapsed Time Difference in Between Scans

One result of study II discovered during our comparison of data from the different instruments was reported previously. Specifically, we observed gross discrepancies between scan time differences and corresponding elapsed time entries in the headers of the data files generated by the ProteomeLab™ XL-A/XL-I Graphical User Interface acquisition software version 6.0 (firmware version 5.06) provided by the manufacturer. Based on independent observations and file time-stamps generated by the computer operating system, this resulted in an underestimate of the true elapsed time, by as much as 10% [40]. We were able to correct for time-stamp errors in the data files by showing that the time-stamps provided by the operating system represent an excellent measure of the passage of time between scans [40].

However, we also noted smaller inconsistencies between file operating system time-stamps and time entries in the file header for data collected using previous versions of the manufacturer's data acquisition software. To further refine the previous work and clarify the origin of these discrepancies, we conducted an SV experiment with an AUC running Beckman Coulter data acquisition software version 5.8 (firmware version 4.21), and determined the true elapsed times by reference to a radio-controlled clock reporting US official time. We compared these values with the elapsed time values reported in the scan file header and the file time-stamps provided by the operating system. In order to be able to assess with good precision even small timing discrepancies, we conducted scans over a time-period of 40 hours. First, we observed that the radio-controlled clock and the file time-stamps provided by the computer operating system were off by 2 seconds after 140,000 sec, a difference of less than 0.002% which can be accepted as sufficiently accurate for any SV experiment. Furthermore, on the instrument tested, the apparent endpoint for absorbance scanning (as judged by the end of lamp flashing) preceded the operating system file time-stamps by a constant value of 15-16 sec; such a delay for the interference data is estimated to be 5 – 7 sec. Even though the scan times reported in the scan log files were correct, coinciding with the operating system computer time, the elapsed time entry of the data files showed an increasing lag from the true elapsed time, amounting to more than 18 min after 40 hours, corresponding to an error of 0.78% (Supplementary Table 2). This lag was essentially identical for the interference and absorbance data, but different for another experiment conducted on the same instrument with different scan settings.

We next examined the file time-stamps and the elapsed time entries from the data acquisition software of the AVIV fluorescence detection system installed on one of our instruments. In this case, the differences did not increase during the run, but varied in a seemingly random manner between -1 and +3 sec, corresponding to an error of 0.0048%, over the entire time course of the data acquisition (Supplementary Table 3). This lends further support to the use of the computer clock as a device to measure the scan times.

We finally examined several XL-A and XL-I SV data sets collected using previous versions of the data acquisition software ranging from 3.01h to 5.7, representing experiments carried

out over the past 15 years in many different instruments. In all cases, file time errors of 0.1 – 2.0% were found. While the source of this error is currently unclear, the largest errors of 1.7 – 2.0% were found in data sets collected at high rotor speeds of 58,000 – 60,000 rpm using version 5.7 (firmware 4.21) of the data acquisition software. This is in contrast to version 6 (firmware 5.06) of the software, where errors were maximal at 50,000 rpm [40]. We are uncertain if these are the only conditions for such large errors to occur, and whether we found examples for the largest possible error. In fact, while the preceding observations were made for SV experiments with interference detection or with absorbance detection using our standard, quick absorbance scan settings, we examined one approach-to-equilibrium experiment where typical equilibrium absorbance scan settings were used and found a time error of 3.6%, pointing to a possible exacerbation of errors at slower scan settings. In all experiments examined, consistent with observations made using the current data acquisition software versions, the scan log files reported scan start times that essentially coincide with the operating system time. However, the elapsed time entries of the scan log files, as well as the header entries of the scan files contained erroneous entries, increasingly lagging (for example, by ~15 min after ~ 14 hours run time) behind the difference between scan start times or time differences between file time stamps. Initial experiments with the newly released firmware version 5.07 indicate that the larger errors of firmware 5.06 are absent. The properties of the recorded scan times now appear to be similar to those observed for firmware versions prior to 5.06, in that small systematic time errors persist.

Measurement of the Radial Magnification

Based on the results from study I, an additional factor that can impact the accuracy of s_{exp}-values is the radial calibration. To identify and correct for such errors, we designed a precision fabricated mask that can be run in a rotor hole along-side the sample and that, when imaged, will create a regular pattern with known distance markers (Figure 1B, C). Even though we cannot independently localize the absolute radial positions of the mask, we can determine relative positions and assess translation and magnification errors. Errors in *s*-values arising from the errors in the radial measurement will depend on the relative error of the radius, as demonstrated above, and therefore, with the sample located at 6 – 7 cm from the distance of rotation, even moderately large errors in absolute position would impact the determined *s*-values very little.

It is useful, though, that the mask stably remains at the same position, such that instrument-to-instrument variations of absolute radial positions can be tracked. Figure 5A shows a superposition of images from the same mask using the absorbance scanner operated in intensity mode (similar scans can be made from the interference data). The scans clearly show the pattern of the mask, with the high signal plateaus representing the spacing between the mask stripes and the low signal plateaus showing the locations of the holes. While clear differences in image position can be discerned, very little difference is observed in replicate experiments in the same instrument (Figure 5B).

One of the most valuable aspects of the mask is that the known distance between the edges provides up to 14 reference markers that can probe both the linearity of the radial imaging, as well as its magnification. Even though it is not entirely clear which feature of the steep increase in transmitted light intensity in the transition regions should be taken as the best estimate for the location of the edge, which might also depend on the focal point and the optics used, one can expect that errors in assignment will occur in the same way for each hole of the mask. For example, we observed that radial points corresponding to the onset of shadow on each side of a hole typically produces a set of points alternating between a slightly larger and slightly smaller radial interval, whereas the spacing of the steepest slopes in the transition typically produces a set of equidistant markers. Either way, along the set of 7 holes, the 14 imaged edges will define the same magnification factor. The results from the

steepest-ascent method best reproduced the equidistant edges for absorbance data in intensity mode. Although one instrument showed indications of weak non-linearity in the radial imaging, for all others the images of the reference points appeared well described as a linear function. An example is shown in Figure 5C. From the slope we can assess errors in the magnification, which is the basis of a radial calibration correction factor, as listed in Table 1. Based on the scatter of these points, typical statistical errors in the determination of the radial calibration correction factor are ~ 0.3%. Within this uncertainty, no significant deformation of the mask as a function of rotor speed was observed although the displacement from rotor stretching is clearly visible (Supplemental Figure 2).

On average, the magnification errors amounted to + 1.2 %, i.e. the image provided a significant underestimate of the distance migrated. Whether this was related to the fact that many runs were carried out with the same counterbalance was not further investigated. In one instrument, the magnification error was significantly larger at ~ 6 - 7 %, without showing any signs of malfunction during operation.

Combined Time Stamp, Scan Velocity, Radial Magnification and Temperature Corrections

Further correction of the $s_{20,\tau}$-values for radial magnification errors utilizing the external radial calibration procedure described above resulted in corrected $s_{20,rad,\tau}$ that exhibited an average of 4.317 S with a standard deviation of ± 0.034 S (0.78%). This represents a 2.5-fold improvement when compared to the values corrected solely for time and temperature, and a 4.2-fold improvement over those only corrected for time.

The improvement from $s_{20,\tau}$-values to $s_{20,rad,\tau}$x-values when applying the additional radial calibration correction can be discerned from a scatter plot of temperature measured with the iButton® *versus* *s*-values with and without radial correction (Figure 6), which exhibits a clear correlation between measured temperature and radially corrected *s*-values. This highlights the importance of combining the two correction factors, and provides independent experimental support for the accuracy of both calibrations.

It is worthwhile to distinguish the effect of radial calibration to the data acquired with the two different optical systems. In the case of the absorbance data, the improvement in precision from external radial calibration is 4.2-fold, going from an $s_{20,\tau}$-value of 4.272 ± 0.110 S to an $s_{20,rad,\tau}$-value of 4.335 ± 0.026 S, with an average magnification error of (1.5 ± 2.4)%. For the Rayleigh interference data a slight decrease of consistency was observed, going from an $s_{20,\tau}$-value of 4.260 ± 0.021 S to an $s_{20,rad,\tau}$-value of 4.292 ± 0.027 S, with an average magnification error of (0.63 ± 0.43)%. Interestingly, magnification errors in the absorbance system, which may arise from variations in the counterbalance, errors in the automatic system calibration and radial scanner mechanism, appear more random than in the interference optics, where the radial calibration is conducted manually and the optical system has no moving parts.

Overall, even though interference and absorbance data gave *s*-values with overlapping 68% confidence intervals, it seems noteworthy that average interference $s_{20,rad,\tau}$-values were slightly lower than average $s_{20,rad,\tau}$-values from the absorbance optics. Significantly, this is true without exception for each run analyzed (Table 1), which clearly shows remaining small systematic differences between the results from the two optical systems. A slight reduction in the differences between the optical systems is achieved by accounting for the finite velocity of the absorbance scanner, which gives the boundary in later scans increasingly more time to migrate before detection. This leads to a systematically increasing over-estimate of the boundary position at the nominal scan time, and thus an overestimate of the sedimentation coefficient. Although this effect is small, nominally at 0.18% for the BSA monomer using the standard scan conditions applied in this study (Eq. 9), it is an obligate

consequence of the finite scan time of the absorbance system and its correction does reduce the discrepancy between the optical systems. The origin of the remaining small difference between the two optical systems is currently unknown. Overall, taken together this leads to a final corrected $s_{20,rad,\tau,\nu}$- value of 4.313 ± 0.031 S, with a relative standard deviation of 0.73%. This is a 2.7-fold improvement when compared to the values corrected solely for time-stamp and temperature, and a 4.5-fold improvement over those only corrected for time-stamp, lending further support to the joint use of both external temperature and radial magnification corrections.

Assessment of Absorbance Linearity and Measurement of Rotor Speed

To complete this study of parameters that could potentially impact the precision of the determined *s*-values we carried out independent measurements of the rotor speed , using a frequency counter, in seven of our instruments with a rotor at 50,000 rpm. The error was typically ~ 0.01% and maximally 0.015% (data not shown), and certainly of sufficient precision for most applications.

Finally, we assessed the linearity of the absorbance optical detection. Theoretically, non-linearity could distort the boundary shapes and lead to errors in the derived sedimentation coefficients. A set of simple absorbance measurements with solutions at expected OD-values of 0.2, 0.6, and 1.0 indicated the absence of any measurable non-linearity (Supplementary Table 4).

Discussion

The accuracy of the *s*-values determined in AUC is of critical importance, especially in hydrodynamic modeling. Translational friction coefficients, being a single number, cannot unambiguously predict a three-dimensional structure, but their accurate determination allows one to readily assess important features of the gross solution structure. For example, due to the relatively narrow bounds that the frictional ratios of folded proteins can assume, it is possible to deduce from the measured frictional coefficients both the oligomeric state and overall shape asymmetry. This information becomes even more valuable when combined with structural models that provide a context in which more detailed question can be asked, such as examining the arrangement of domains for which atomic coordinates are available, or, evaluating ensembles of solution structures derived from small angle X-ray or neutron scattering curves.

This approach is becoming more attractive as the hydrodynamic modeling translating atomic coordinates into the space of frictional coefficients is getting more precise [31], coincident with the increase in resolution and statistical precision provided for by the computational analysis of SV data. Due to the near ubiquitous presence of degradation products in most protein samples, if not heterogeneity from multiple native states, improvements in hydrodynamic resolution have a particularly high impact on the reliability and usefulness of the measured *s*-values for hydrodynamic interpretation. In practice, this often offers a significant advantage over other hydrodynamic techniques such as dynamic light scattering. On the other hand, any measurement in AUC introduces the density increment as a parameter, since sedimentation will depend on the macromolecular buoyancy. We have recently developed a density contrast SV approach using global modeling of experiments at different solvent densities carried out side-by-side in the same run, that allows for the determination of macromolecular partial-specific volumes with a precision better than 0.5% [60]. For proteins, this will propagate as an error of ~ 1.5% in the buoyant molar mass. In particular after applying the external calibration corrections described in the present paper, this will remain the dominant source of uncertainty in the determination of translational frictional coefficients. Thus, we agree with Errington & Rowe that the most powerful use of

hydrodynamic information from SV arises in the measurement of relative changes in *s*-values [42], for example, from conformational changes, where error contributions from the density increment cancel out.

Furthermore, hydrodynamic modeling needs to account for protein hydration, and average degrees of hydration have been inferred from the measured transport properties of a set of 'calibrating' proteins of known structure [32,61]. Therefore, when compared to the expected errors in the data interpretation, instrument to instrument variation of measured *s*-values of ~ 10% recently reported [46], and the variations of similar magnitude found in the present study for uncorrected *s*-values, are highly problematic.

The set of controls proposed in the present work involves a standard for the sedimentation coefficient, a new approach for measuring the spatial accuracy of the AUC, the use of the independent computer clock for more accurate scan times, and a device that allows for an independent measurement of the rotor temperature. These controls are inexpensive, stable, independent of manufacturer calibration or instrument modifications, and can be conveniently performed as auxiliary experiments side-by-side to the experiments of interest.

We have already reported our approach for correcting erroneous run times in the data files by reading the external time-stamp provided by the computer operating system, a necessity that arose from the present study after elimination of the other factors, and is accomplished automatically in current versions of the SEDFIT software [40]. In a refinement of the previous work [40] that reported gross errors in the scan time entries in the headers of files generated by the most current data acquisition software and/or its associated ultracentrifuge firmware deployed by the manufacturer for nearly two years, we found a similar, but smaller error with use of previous versions of the data acquisition software. Use of the Beckman-Coulter ProteomeLab™ version 5.8 resulted in a time error of 0.78%. Furthermore, when examining earlier data sets spanning the last decade and a half, we consistently observed elapsed time errors of 0.1% - 2.0%, indicating that s-values in the literature may have been systematically overestimated by a significant amount, possibly since the introduction of the Beckman Optima XL-A analytical ultracentrifuge. Errors of the order of 0.1% may have been negligible when using previous data analysis methods, although they exceed the uncertainty of current Lamm equation modeling approaches. However, errors in excess of 1%, such as the values of 1.7%–2.0% found for software version 5.7 at 59,000 rpm, are of significant concern. Given that these errors correspond to an obvious lag of many minutes over the time course of a typical SV experiment and given that time entries reported in the scan log files generated by the data acquisition software seem to reflect the correct times, it is surprising both that such an error can occur and that it has not been discovered previously. Our findings demonstrate the need for critical inspection even of basic parameters reported by scientific instruments [62].

We have demonstrated in the present work that it is advantageous to rely on the operating system time-stamps of the scan files, which is of sufficient precision and trivial to obtain. This assumes that no dramatic systematic variation in the other processes requiring processor time occurs, which in our experience can be simply ensured by not utilizing the same computer for other purposes during data acquisition. In this case, the delay between the end of the scan and the creation of the data file is typically on the order of 10 seconds and constant throughout the experiment. Variations on the order of a couple of seconds were observed (as can be discerned, for example, in the data files from the fluorescence optical data acquisition software by AVIV, Supplementary Table 3), but are without consequence on the time-scale of sedimentation experiments. We make the assumption that the same time dilation errors occur proportionally during the time between the start of the centrifuge and the first scan. Any deviation from this can be absorbed into the best-fit meniscus position

during the data analysis, similar to other errors in the effective start time [25]. Therefore, the absolute time of scan is irrelevant for the scan time dilation corrections, and only differences in the scan times need to be assessed.

A smaller timing related error, also leading to systematic overestimates, is the effect of the finite absorbance scanner velocity that allows more time for signals at higher radial values prior to absorbance detection [20]. After measuring the scan velocity, the effect of this on the *s*-values can be calculated, or this effect can be mimicked directly when calculating Lamm equation solutions corresponding to experimental scans [20]. This correction would be significantly more convenient if absorbance scan files were to report correct elapsed times associated with each single data point. In the absence of such time information, we can make approximate corrections based on the average linear velocity of the scanner measured for given scan settings.

After the time correction, the most critical and difficult calibration is that for temperature. The issue of the sample's actual temperature in the spinning rotor, and the controversies arising from different hydrodynamic results on the basis of temperature and different methods for temperature calibration, has a history almost as long as that of the AUC. For modern ultracentrifuges, a temperature accuracy and stability better than ± 0.1°C was stated by Laue & Stafford [63], but this appears to be quite unrealistic in common practice, considering, the instrument specifications of ± 0.5 °C by the manufacturer.

The importance of temperature calibration has previously been emphasized by Liu & Stafford [49], who proposed a method for external temperature calibration based on the strongly temperature-dependent spectral change of $CoCl_2 \cdot 6H_2O$ in water/ethanol solutions [64], previously used for optical temperature measurement in other techniques [65,66]. Similar to the procedure described in the present work, it can only be used at low rotor speeds, due to a strong pressure and solvent composition dependence of the thermochromic shift [49,67]. With a relative change of the spectral area of only ∼ 4% per °C at room temperature inferred from Figure 2 of [49], this method is very demanding on the photometric accuracy of both the reference benchtop spectrophotometer and the AUC absorbance scanner. The bench-top spectrophotometer used in [49] is specified by the manufacturer to be accurate to ± 0.005 AU at 1 AU [69], or 0.5% which would translate to an error in possible temperature accuracy of > 0.1 °C, prior to any other considerations. A photometric certification for the AUC is offered by the manufacturer only as a non-standard procedure, which will currently guarantee the accuracy of absorbance readings to within ± 0.025 AU at an absorbance of 0.06 AU, and ± 0.045 AU at an absorbance of 1.0 AU (consistent with our absorbance data in Supplementary Table 4). This amounts to an uncertainty in excess of 4.5%, which would propagate into an additional temperature uncertainty from this factor alone of at least 1.0 °C. In addition, we estimate that a constant baseline offset of only 0.005 AU across the spectrum (consistent with the systematic radial-dependent offsets described in [22, 68]) could translate in systematic errors of ∼ 0.25 °C in temperature at 20.0 °C. Liu & Stafford have not independently validated the temperature measurements, and considered only stochastic errors of the absorbance spectra, arriving at an estimated uncertainty in temperature for their colorimetric method of ∼ 0.04 °C at 20.0 °C, and reported a standard error from short-term repeatability of ∼ 0.01 °C [67]. However, compared to the latter value, after accounting for all error propagation from baselines and photometric calibrations in current instruments, temperature uncertainties in such measurements would be approximately two orders of magnitude larger. In fact, they are at a level where it seems that the colorimetric method could potentially cause temperature uncertainties even larger than the manufacturer's specifications. It is conceivable that the method by Liu & Stafford [49] could be improved by a photometric calibration, but such a procedure has not been described in the literature and was not attempted in the present work.

Instead, we have pursued a more direct temperature measurement, continuing the strategy of thermistors located in the rotor [53,56], by using modern inexpensive computer chips that can be gently centrifuged while autonomously logging the rotor temperature. We have supported the temperature corrections to the instrument calibration by independent hydrodynamic measurements of the ensuing effect on the solvent viscosity with simultaneous radial magnification corrections (Figure 6). Even though the temperature calibration for different instruments seems to be stable and usually within the manufacturer's specification, in two of our instruments sudden changes were observed, which suggests that a periodic test of the temperature accuracy is necessary, even when the instrument is covered under a standard service contract. In our experiments, the actual temperatures measured at the same nominal temperature of 20 °C varied by ∼ 4 °C for the instruments under study.

Adiabatic cooling of the rotor upon acceleration is an additional factor that transiently impacts rotor temperature early in the run. Unfortunately, our digital temperature loggers cannot withstand the high gravitational fields so that we could not directly measure this effect. However, with the titanium rotors currently in use this effect should be small, based on their smaller coefficient of expansion and lower specific heats than the historic aluminum rotors [70]. In fact, much like our observations when setting up sedimentation velocity experiments, Gropper and Boyd have demonstrated that titanium rotors transiently cool by 0.2 – 0.3 °C when accelerated to 68,000 rpm – fivefold less than with aluminum rotors, which should make this factor negligible in current practice [70].

An additional large source of error can be the radial calibration. Using the mask we could determine the magnification with a precision of ∼ 0.3%, and found calibration errors ranging from −1.2% to −7.4% in our set of experiments. This has previously not been recognized as such a significant source of error, and no alternative external calibrations have been described in the literature. Importantly, this error will affect sedimentation velocity and equilibrium experiments alike, and would go unnoticed without external control. The current standard method is a two-point calibration based on slits in the counterbalance. Previously, using the laser interferometer we have compared the images of these calibration slits in six counterbalances placed side-by-side in the same rotor, and found standard deviations of 30 – 40 μm, also corresponding to a maximum magnification error of ∼0.3% [20]. The fact that the external magnification corrections with the mask improve on the standard calibration suggests that in the latter additional errors are introduced both by the operator in carrying out the manual calibration of the interference optical system, as well as in the automated calibration of the absorbance system. An additional benefit of the use of the mask is that it allows for the visualization of additional instrumental problems that may easily go unnoticed. For example, we observed significant intensity changes across the radial range in one instrument, and significant out-of-focus alignment in another, both leading to subsequent service repairs.

The rotor speed may also be another issue of concern, and based on instrument specifications of ± 20 rpm at 50,000 rpm, errors of ± 0.08% in the sedimentation coefficient could arise. However, we measured a much smaller error of typically ∼ 0.01%. As expected, this is sufficiently precise not to be limiting. Finally, we have no indications that signal non-linearity occurs in the concentration range studied although this could theoretically lead to errors in *s*-values. This covers all data dimensions of AUC data and basic centrifugal quantities required for their interpretation.

The need for the combined application of the radial, temporal, and thermal calibration corrections becomes clear in Figure 7, which displays a visual summary of the measured *s*-values before and after individual and joint calibrations. The fact that each calibration correction, when applied separately, does not produce a narrow set of *s*-values has probably

hampered the recognition of their importance. In particular, even though the large shift from scan time errors seems obvious in retrospect, they might have been obscured by contributions from thermal and radial errors which may have delayed their discovery. Thermal corrections are most effective in tightening the 25 to 75 percentile of the distribution, but clearly all corrections are needed for truly quantitative measurements.

The remaining standard deviation of 0.73 % for the BSA monomer observed in different instruments in our study is still larger than the reproducibility of 0.37 % reported by Errington & Rowe for 20 replicate runs of a 42 S vaccine sample [42]. This may be related to a dependency of the precision on the size or *s*-value of the material under study, and/or be related to the different number of instruments sampled in the present study. The remaining error is also significantly larger than the precision of relative *s*-values measured side-by-side in the same run, which was previously estimated to be < 0.1% [42], and in the present study found to be only slightly worse at 0.15%. This clearly demonstrates the remaining imperfection of the calibration, despite the improvements from the external radial and temperature calibration. Obviously, errors can be much larger if unrecognized instrumental malfunctions are present, or due to various imperfections in the experiment, such as convection from the lack of temperature equilibration or centerpiece sector alignment.

In this regard, we have come to the recognition that conducting periodic control experiments with an *s*-value standard is indispensable. We found BSA dissolved in phosphate buffered saline to be a suitable sample, as it is very stable with time, and can be resuspended easily after each run. Formation of oligomers is not problematic as they can be clearly baseline-separated in the $c(s)$ analysis. Importantly, this BSA is commercially available, inexpensive, and does not require further expertise in protein purification. The dissolved sample can be left in a cell assembly and stored in the refrigerator at 4°C over months. Other options include aldolase, which has been used previously as a stable reference protein in studies of hydration [71]. Such a control run can be preceded by temperature measurements with the iButton® and be accompanied by scans of a constant reference cell assembly with radial calibration mask.

In order to improve on the current study of the accuracy and reproducibility of measuring sedimentation coefficients, it would be useful in future work to expand the number of instruments and laboratories studying the same sample employing the same protocols and carrying out accompanying control experiments for temperature with an iButton® and for radial magnification with an identical mask.

Supplementary Material

Refer to Web version on PubMed Central for supplementary material.

Acknowledgments

We thank Erby Perdue for his expert advice and for taking excellent care of our analytical ultracentrifuges, and Dr. Nicole Morgan for helpful discussions. This work was supported by the Intramural Research Programs of the National Institute of Biomedical Imaging and Bioengineering, the National Institute of Diabetes and Digestive and Kidney Diseases, and the National Heart, Lung and Blood Institute, National Institutes of Health.

References

1. Howlett GJ, Minton AP, Rivas G. Analytical ultracentrifugation for the study of protein association and assembly. Curr Opin Chem Biol. 2006; 10:430–436. [PubMed: 16935549]
2. Schuck P, Zhao H. Editorial for the special issue of methods “Modern Analytical Ultracentrifugation”. Methods. 2011; 54:1–3. [PubMed: 21536133]

3. Arisaka F. Applications and future perspectives of analytical ultracentrifugation. Tanpakushitsu Kakusan Koso. 1999; 44:82–91. [PubMed: 10025175]
4. Harding SE, Rowe AJ. Insight into protein-protein interactions from analytical ultracentrifugation. Biochem Soc Transact. 2010; 38:901–7.
5. Trautman R. The impact of the desk-top computer on ultracentrifugation. Ann N Y Acad Sci. 1969; 164:52–65.
6. Cox DJ. Computer simulation of sedimentation in the ultracentrifuge I. Diffusion. Arch Biochem Biophys. 1965; 112:249–258.
7. Crepeau RH, Conrad RH, Edelstein SJ. UV laser scanning and fluorescence monitoring of analytical ultracentrifugation with an on-line computer system. Biophys Chem. 1976; 5:27–39. [PubMed: 963221]
8. Yphantis DAA. Equilibrium ultracentrifugation of dilute solutions. Biochemistry. 1964; 3:297–317. [PubMed: 14155091]
9. Gilbert GA, Gilbert LM. Ultracentrifuge studies of interactions and equilibria: impact of interactive computer modelling. Biochem Soc Trans. 1980; 8:520–522. [PubMed: 7450200]
10. Furst A. The XL-I analytical ultracentrifuge with Rayleigh interference optics. Eur Biophys J. 1997; 25:307–310.
11. Giebeler, R. The Optima XL-A: A new analytical ultracentrifuge with a novel precision absorption optical system. In: Harding, SE.; Rowe, AJ.; Horton, JC., editors. Analytical Ultracentrifugation in Biochemistry and Polymer Science. Cambridge, U.K.: The Royal Society of Chemistry; 1992. p. 16-25.
12. Brown PH, Schuck P. A new adaptive grid-size algorithm for the simulation of sedimentation velocity profiles in analytical ultracentrifugation. Comput Phys Commun. 2007; 178:105–120. [PubMed: 18196178]
13. Dam J, Velikovsky CA, Mariuzza R, Urbanke C, Schuck P. Sedimentation velocity analysis of protein-protein interactions: Lamm equation modeling and sedimentation coefficient distributions c(s). Biophys J. 2005; 89:619–634. [PubMed: 15863475]
14. Stafford WF, Sherwood PJ. Analysis of heterologous interacting systems by sedimentation velocity: curve fitting algorithms for estimation of sedimentation coefficients, equilibrium and kinetic constants. Biophys Chem. 2004; 108:231–43. [PubMed: 15043932]
15. Schuck P. Sedimentation analysis of noninteracting and self-associating solutes using numerical solutions to the Lamm equation. Biophys J. 1998; 75:1503–1512. [PubMed: 9726952]
16. Schuck P. Size-distribution analysis of macromolecules by sedimentation velocity ultracentrifugation and lamm equation modeling. Biophys J. 2000; 78:1606–1619. [PubMed: 10692345]
17. Brown PH, Schuck P. Macromolecular Size-And-Shape Distributions by Sedimentation Velocity Analytical Ultracentrifugation. Biophys J. 2006; 90:4651–4661. [PubMed: 16565040]
18. Balbo A, Minor KH, Velikovsky CA, Mariuzza R, Peterson CB, Schuck P. Studying multi-protein complexes by multi-signal sedimentation velocity analytical ultracentrifugation. Proc Nat Acad Sci USA. 2005; 102:81–86. [PubMed: 15613487]
19. Schuck P, Taraporewala ZF, McPhie P, Patton JT. Rotavirus nonstructural protein NSP2 self-assembles into octamers that undergo ligand-induced conformational changes. J Biol Chem. 2001; 276:9679–87. [PubMed: 11121414]
20. Brown PH, Balbo A, Schuck P. On the analysis of sedimentation velocity in the study of protein complexes. Eur Biophys J. 2009; 38:1079–1099. [PubMed: 19644686]
21. Zhao H, Brown PH, Balbo A, Fernandez Alonso MC, Polishchuck N, Chaudhry C, Mayer ML, Ghirlando R, Schuck P. Accounting for solvent signal offsets in the analysis of interferometric sedimentation velocity data. Macromol Biosci. 2010; 10:736–745. [PubMed: 20480511]
22. Schuck P, Demeler B. Direct sedimentation analysis of interference optical data in analytical ultracentrifugation. Biophys J. 1999; 76:2288–2296. [PubMed: 10096923]
23. Schuck P. A model for sedimentation in inhomogeneous media. I. Dynamic density gradients from sedimenting co-solutes. Biophys Chem. 2004; 108:187–200. [PubMed: 15043929]

24. Gabrielson JP, Arthur KK, Kendrick BS, Randolph TW, Stoner MR. Common excipients impair detection of protein aggregates during sedimentation velocity analytical ultracentrifugation. J Pharm Sci. 2009; 98:50–62. [PubMed: 18425806]
25. Besong TMD, Harding SE, Winzor DJ. The effective time of centrifugation for the analysis of boundary spreading in sedimentation velocity experiments. Anal Biochem. 2012; 421:755–8. [PubMed: 22197415]
26. Pekar AH, Sukumar M. Quantitation of aggregates in therapeutic proteins using sedimentation velocity analytical ultracentrifugation: practical considerations that affect precision and accuracy. Anal Biochem. 2007; 367:225–237. [PubMed: 17548043]
27. Balbo A, Zhao H, Brown PH, Schuck P. Assembly, loading, and alignment of an analytical ultracentrifuge sample cell. J Vis Exp. 2009
28. Zhao H, Brautigam CA, Ghirlando R, Schuck P. Current methods in sedimentation velocity and sedimentation equilibrium analytical ultracentrifugation. Curr Protoc Protein Sci. 2013; 7:20.12.1.
29. Salvay AG, Communie G, Ebel C. Sedimentation velocity analytical ultracentrifugation for intrinsically disordered proteins. Methods Mol Biol. 2012; 896:91–105. [PubMed: 22821519]
30. le Maire M, Arnou B, Olesen C, Georgin D, Ebel C, Møller JV. Gel chromatography and analytical ultracentrifugation to determine the extent of detergent binding and aggregation, and Stokes radius of membrane proteins using sarcoplasmic reticulum Ca2+-ATPase as an example. Nat Protoc. 2008; 3:1782–1795. [PubMed: 18974737]
31. Aragon SR. Recent advances in macromolecular hydrodynamic modeling. Methods. 2011; 54:101–14. [PubMed: 21073955]
32. Aragon SR, Hahn DK. Precise boundary element computation of protein transport properties: Diffusion tensors, specific volume, and hydration. Biophys J. 2006; 91:1591–1603. [PubMed: 16714342]
33. Rai N, Nöllmann M, Spotorno B, Tassara G, Byron O, Rocco M. SOMO (Solution MOdeler) differences between X-Ray- and NMR-derived bead models suggest a role for side chain flexibility in protein hydrodynamics. Structure. 2005; 13:723–734. [PubMed: 15893663]
34. Harding SE, Longman E, Carrasco B, Ortega A, Garcia de la Torre JG. Studying antibody conformations by ultracentrifugation and hydrodynamic modeling. Methods Mol Biol. 2003; 248:93–113. [PubMed: 14970492]
35. Ortega A, Amorós D, García de la Torre J. Prediction of hydrodynamic and other solution properties of rigid proteins from atomic- and residue-level models. Biophys J. 2011; 101:892–8. [PubMed: 21843480]
36. Perkins SJ, Nan R, Li K, Khan S, Abe Y. Analytical ultracentrifugation combined with X- ray and neutron scattering: Experiment and modelling. Methods. 2011; 54:181–99. [PubMed: 21256219]
37. Wohlleben W. Validity range of centrifuges for the regulation of nanomaterials: from classification to as-tested coronas. J Nanopart Res. 2012; 14:1300. [PubMed: 23239934]
38. Berkowitz SA. Role of analytical ultracentrifugation in assessing the aggregation of protein biopharmaceuticals. AAPS J. 2006; 8:E590–605. [PubMed: 17025277]
39. Gabrielson JP, Arthur KK. Measuring low levels of protein aggregation by sedimentation velocity. Methods. 2011; 54:83–91. [PubMed: 21187149]
40. Zhao H, Ghirlando R, Piszczek G, Curth U, Brautigam Ca, Schuck P. Recorded Scan Times Can Limit the Accuracy of Sedimentation Coefficients in Analytical Ultracentrifugation. Anal Biochem. 2013 in press. 10.1016/j.ab.2013.02.011
41. Cecil R, Ogston AG. The accuracy of the Svedberg oil-turbine ultracentrifuge. Biochem J. 1948; 43:592–8. [PubMed: 16748457]
42. Errington N, Rowe AJ. Probing conformation and conformational change in proteins is optimally undertaken in relative mode. Eur Biophys J. 2003; 32:511–517. [PubMed: 12830332]
43. Boukari H, Nossal RJ, Sackett DL, Schuck P. Hydrodynamics of nanoscopic tubulin rings in dilute solution. Phys Rev Lett. 2004; 93:98106.
44. Werner WE, Cann JR, Schachman HK. Boundary Spreading in Sedimentation Velocity Experiments on Partially Liganded Aipartate Transcarbamoylase. J Mol Biol. 1989; 206:231–237. [PubMed: 2649685]

45. Bayliss RI, Errington N, Byron O, Svensson A, Rowe AJ, Svensson RIBA, Le L. A conformation spectrum analysis of the morphological states of myosin S1 in the presence of effectors. Coll Polym Sci. 1999; 113:158–163.
46. Zhao H, Berger AJ, Brown PH, Kumar J, Balbo A, May CA, Casillas E, Laue TM, Patterson GH, Mayer ML, Schuck P. Analysis of high-affinity assembly for AMPA receptor amino-terminal domains. J Gen Physiol. 2012; 139:371–388. [PubMed: 22508847]
47. MacGregor IKK, Anderson ALL, Laue TM. Fluorescence detection for the XLI analytical ultracentrifuge. Biophys Chem 108. 2004:165–185.
48. Biancheria A, Kegeles G. Thermodynamic measurements of ultracentrifuge rotor temperature. J Am Chem Soc. 1954; 76:3737–3741.
49. Liu S, Stafford WF. An optical thermometer for direct measurement of cell temperature in the Beckman instruments XL-A analytical ultracentrifuge. Anal Biochem. 1995; 224:199–202. [PubMed: 7710072]
50. Incardona NL, Notarius H, Flanegan JB. Measurement of temperature within the sample cell during sedimentation velocity experiments. Anal Biochem. 1971; 40:267–280. [PubMed: 5551540]
51. Rowe AJ, Khan GM. Determination of Corrected Sedimentation Coefficient at Different Temperatures Using the MSE Analytical Ultracentrifugation. Anal Biochem. 1972; 45:488–497. [PubMed: 5062191]
52. Svedberg, T.; Pedersen, KO. The ultracentrifuge. London: Oxford University Press; 1940.
53. Robinson TK, Beams JW. Radio Telemetering from Magnetically Suspended Rotors. Rev Sci Instrum. 1963; 34:63.
54. Ecker PG, Blum J, Hiatt CW. A Device for the Measurement of Rotor Temperature in the Air-Driven Ultracentrifuge. Rev Sci Instrum. 1949; 20:799. [PubMed: 15395395]
55. Waugh DF, Yphantis DA. Rotor Temperature Measurement and Control in the Ultracentrifuge. Rev Sci Instrum. 1952; 23:609.
56. Fabricant SJ. Ultracentrifuge Rotor Temperature Measurements and Control. Rev Sci Instrum. 1966; 37:495. [PubMed: 5909380]
57. Smith AD, Crabtree DR, Bilzon JLJ, Walsh NP. The validity of wireless iButtons and thermistors for human skin temperature measurement. Physiol Meas. 2010; 31:95–114. [PubMed: 19940348]
58. Lamm O. Die Differentialgleichung der Ultrazentrifugierung. Ark Mat Astr Fys. 1929; 21B(2):1–4.
59. Gropper L. Optical alignment procedure for the analytical ultracentrifuge. Anal Biochem. 1964; 428:401–428. [PubMed: 14165464]
60. Brown PH, Balbo A, Zhao H, Ebel C, Schuck P. Density contrast sedimentation velocity for the determination of protein partial-specific volumes. PLoS One. 2011; 6:e26221. [PubMed: 22028836]
61. García De La Torre J, Huertas ML, Carrasco B. Calculation of hydrodynamic properties of globular proteins from their atomic-level structure. Biophys J. 2000; 78:719–730. [PubMed: 10653785]
62. Jakoby W. Recorded Scan Times Can Limit the Accuracy of Sedimentation Coefficients in Analytical Ultracentrifugation. Anal Biochem. 2013; 437:103. [PubMed: 23454282]
63. Laue TM, Stafford WF. Modern applications of analytical ultracentrifugation. Annu Rev Biophys Biomol Struct. 1999; 28:75–100. [PubMed: 10410796]
64. Day JH. Thermochromism of inorganic compounds. Chem Rev. 1968; 68:649–657.
65. Wätzig H. The measurement of temperature inside capillaries for electrophoresis using thermochromic solutions, Chromatographia. 1992; 33:445–448.
66. Bacci M, Brenci M, Conforti G, Falcial R, Mignani AG, Scheggi AM. Thermochromic transducer optical fiber thermometer. Applied Optics. 1986; 25:1079. [PubMed: 18231301]
67. Johnson JB, Becker K, Edwards G. Pressure corrections for CoCl2 as a thermometer in an analytic ultracentrifuge. Anal Biochem. 1995; 227:385–7. [PubMed: 7573961]

68. Vistica J, Dam J, Balbo A, Yikilmaz E, Mariuzza RA, Rouault TA, Schuck P. Sedimentation equilibrium analysis of protein interactions with global implicit mass conservation constraints and systematic noise decomposition. Anal Biochem. 2004; 326:234–256. [PubMed: 15003564]

69. DU ® Series 600 and 7000 UV/Vis Spectrophotometer Systems. Beckman Instruments; Fullerton, CA: 1997.

70. Gropper L, Boyd W. Temperature measurement and control of analytical rotors in the ultracentrifuge. Anal Biochem. 1965; 11:238–45. [PubMed: 5840658]

71. Ebel C, Eisenberg H, Ghirlando R. Probing protein-sugar interactions. Biophys J. 2000; 78:385–393. [PubMed: 10620302]

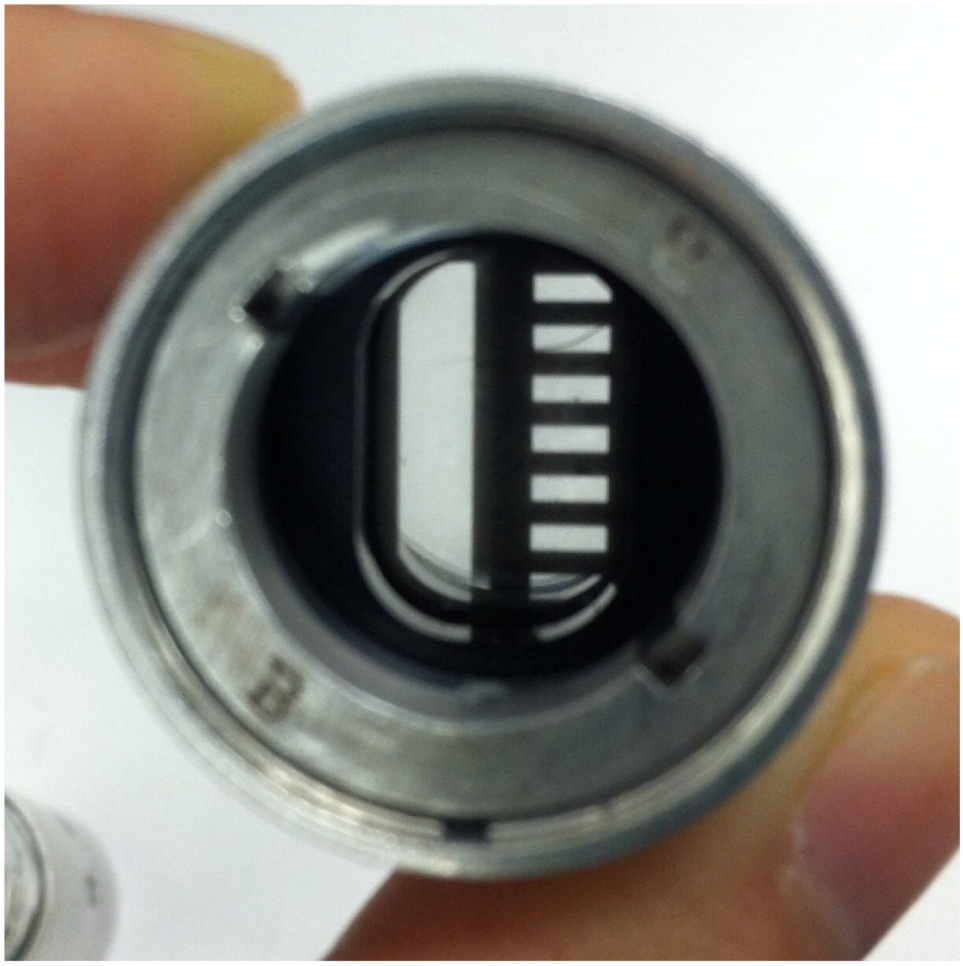

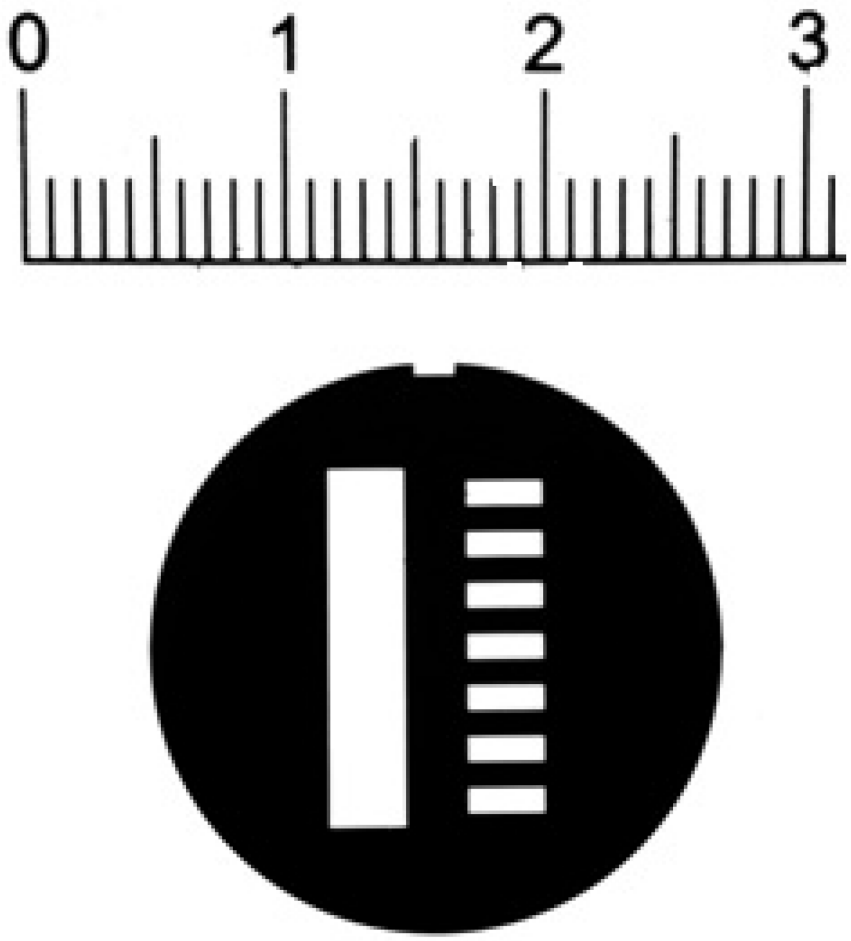

Figure 1.

(**A**) An image of the Thermochron iButton® temperature logger placed in the specially designed aluminum holder and AUC cell housing. The cell is placed such that the 135° orientation faces away from the center of rotation. (**B**) An image of the radial mask placed within the AUC cell housing by sandwiching between two AUC windows. (**C**) The radial mask showing the reference sector on the left and sample sector on the right. The notch for alignment with the cell housing is shown on the top. The ruler shows distances in cm.

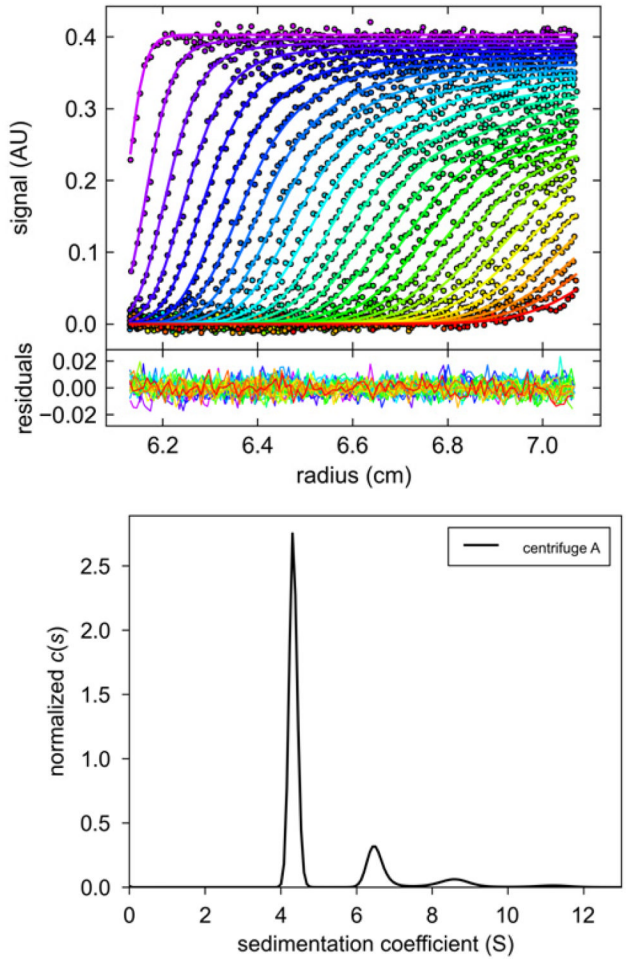

Figure 2.

(**A**) Representative absorbance scans of the sedimentation velocity data of BSA (symbols, showing only every 3rd data point of every 3rd scan), and best-fit boundary model from the *c*(*s*) analysis in SEDFIT (solid lines). (**B**) Residuals of the fit, with a root-mean-square deviation of 0.0054 OD. (**C**) Best-fit sedimentation coefficient distribution *c*(*s*). Figure created with GUSSI, reproduced from [40].

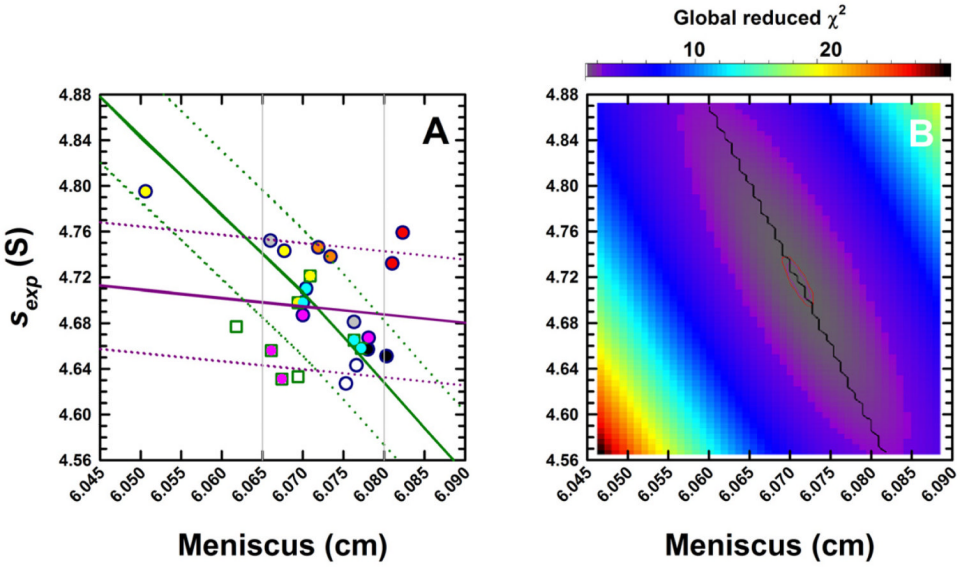

Figure 3.

(**A**) Experimental sedimentation coefficients for monomeric BSA obtained from eight analytical ultracentrifuges in study I, plotted as a function of the best-fit meniscus position. Experiments were conducted in duplicate and data obtained from Cell 1 for the different centrifuges are shown in unique colors. Absorbance (round symbols) and, when possible, interference (square symbols) data were collected. As Version 6.0 (Firmware 5.06) of the ProteomeLab XL/I acquisition software was used in all ultracentrifuges, sedimentation coefficients are ~ 10% larger than the true value. Using the average best-fit *s*-value of the BSA monomer and meniscus position, a set of sedimentation velocity data were simulated in SEDFIT. The solid green line shows how a fixed meniscus position influences the best-fit *s*-value in a *c*(*s*) analysis. Simulated SV data were radially translated to simulate translation errors δr in the radius. The solid purple line shows how such errors influence the sedimentation coefficient. Dotted green and purple lines show s-values if the temperature were changed by ± 0.5 °C. (B) Simulated data were analyzed in SEDPHAT in terms of a single non-interacting ideal solute. The error surface depicting the global reduced χ^2 as a function of the *s*-value and fitted meniscus position shows a well defined minimum.

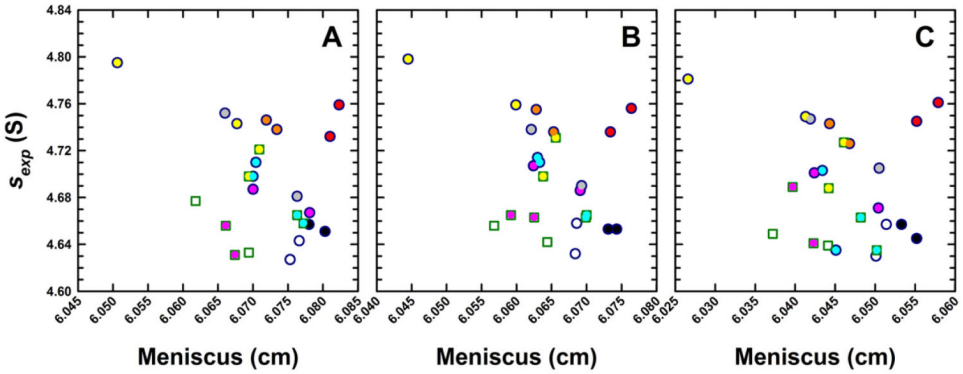

Figure 4.

Experimental sedimentation coefficients for monomeric BSA obtained from eight analytical ultracentrifuges in study I plotted as a function of the best-fit meniscus position. Panels show data obtained from (**A**) Cell 1, (**B**) Cell 2 and (**C**) Cell 3 of identical runs illustrating consistencies in data collected from the same ultracentrifuge. The same instrument color coding is used for each cell and the complete data set is listed in Supplementary Table 1.

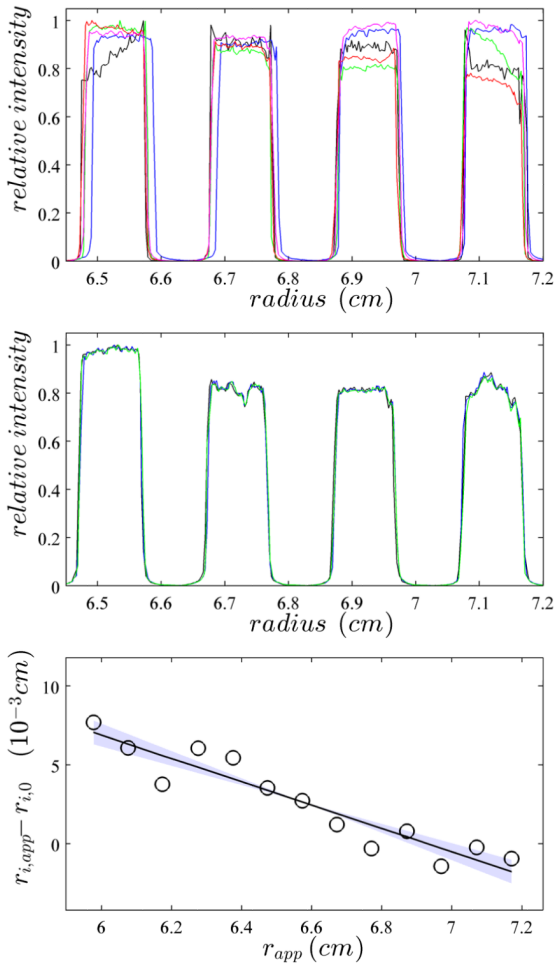

Figure 5.

Calibration of the radial magnification through imaging of the mask. (**Top**) Overlay of the absorbance intensity scans of the mask obtained from five different centrifuges at 50,000 rpm. The same cell assembly with mask was run in all instruments, without disassembly. For clarity, only a subset of the image is displayed that shows only 4 of the 7 calibration holes. (**Middle**) Analogous overlay of mask images from repeat experiments from the same instrument. (**Bottom**) To determine the edges of the calibration holes, 10 replicate scans of the mask are analyzed and the apparent radial position of the average steepest ascent, $r_{i,app}$, are determined. The spacing between the $r_{i,app}$ is compared to the expected spacing of 1.0011 mm, and plotted as the difference of all $r_{i,app}$ positions to the best-fit edge positions constraining their distance to be 1.0011 mm, $r_{i,0}$ (circles). The solid line indicates the best linear fit through $r_{i,app} - r_{i,0}$, in this case corresponding to an imaged edge spacing of 0.09938 cm. The light colored area indicates the 68% confidence region corresponding to edge distances from 0.09925 cm to 0.09950 cm.

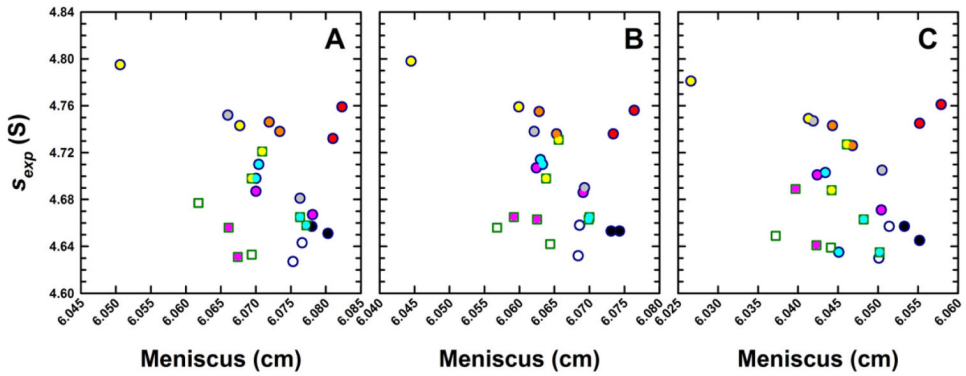

Figure 6.

Effect of external temperature and radial calibration on the measured sedimentation coefficients of the BSA monomer, all acquired at a nominal run temperature of 20 °C with the absorbance optical system. Shown are the measured time-corrected $s_{exp,\tau}$-values prior to radial magnification correction (green asterisks), and the corresponding $s_{\mathrm{rad},\tau}$-values after radial magnification correction (blue solid circles), respectively, plotted against the actual rotor temperature measured with the Thermochron iButton®. The lines represent the theoretical temperature-dependence, accounting for water viscosity, based on the average $s_{20,\,rad,\,\tau}$–value of 4.333 S for all absorbance data shown including radial corrections (blue), and based on the average $s_{20,\,\tau}$–value of 4.294 S for all absorbance data excluding radial corrections (green). The horizontal grey line indicates the average s_{τ}–value of 4.195 S for all absorbance data with neither temperature nor radial magnification corrections, as would be presumed based on the manufacturer's temperature and radial calibration at the used settings of 20 °C for all experiments.

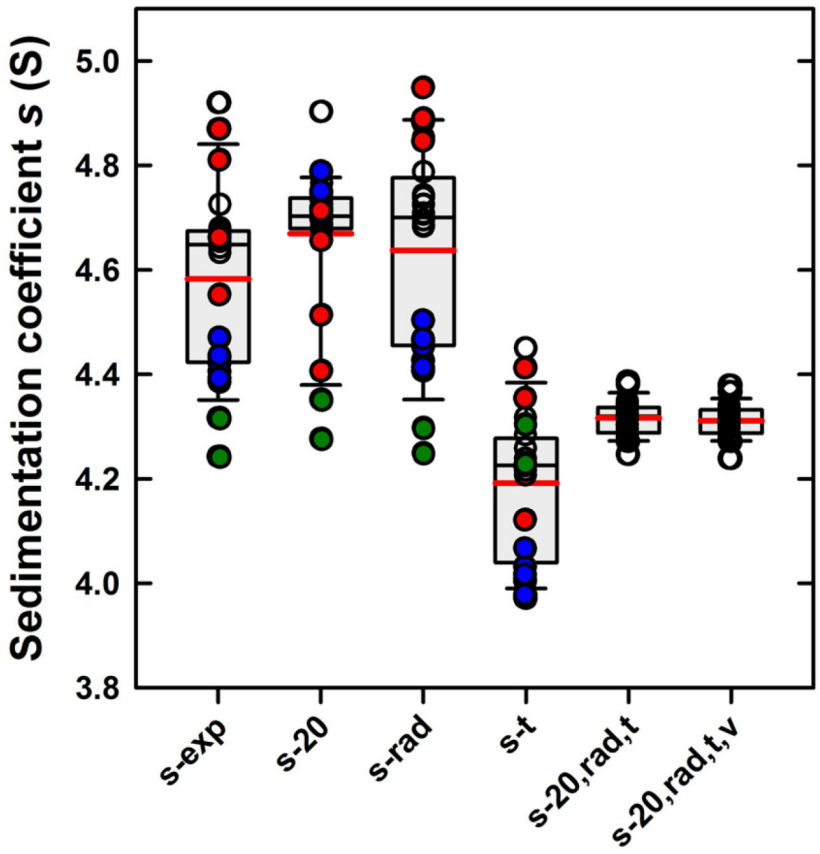

Figure 7.

Box-and-whisker plot (SigmaPlot) of the *s*-values before and after external calibration corrections. For each set, the size of the grey box represents the lower and upper quartiles (25^{th}-75^{th} percentile) of the data set (Table 1). The bold red line represents the mean and the thinner black line the median. Whiskers, calculated using the standard method, represent the 10^{th} and 90^{th} percentiles in the data. Outliers represent the remaining 20 percent of the data are shown individually. All data are shown as circles and bars are labeled as in Table 1: s_{exp} for the experimental *s*-values prior to any corrections, s_{20} for the values corrected solely for temperature, s_{rad} for the values corrected solely for radial magnification errors, s_t for values subjected to scan time corrections, $s_{20,rad,t}$ for values corrected simultaneously for temperature, radial magnification, and scan times, and finally $s_{20,rad,t,v}$ further corrected for the absorbance finite scanning times . Data for Larry and Shemp, which show temperature extremes, are highlighted in red and blue, respectively. The latter instrument also shows the largest radial magnification errors. Data for Clotho with the smallest scan-time errors are shown in green.

Table 1

Sedimentation coefficients measured on ten analytical ultracentrifuges, with and without corrections for temperature, radial magnification, time-stamp errors and scan velocity.

Centrifuge	T (°C)	s_{exp} (S)	visc factor (%)	s_{20} (S)	rad mag factor (%)	s_{rad} (S)	Time factor[a] (%)	s_{τ} (S)	$s_{20,rad,\tau}$ (S)	$s_{20,rad,\tau,v}$ (S)
Larry526b_IF	17.15	4.405	7.11	4.718	0.48	4.426	9.93	4.007	4.312	4.312
Larry526b_280	17.15	4.431	7.11	4.746	0.73	4.463	9.93	4.031	4.349	4.341
Larry526_260	17.15	4.47	7.11	4.788	0.73	4.503	9.93	4.066	4.387	4.379
Larry528_IF	17.15	4.385	7.11	4.697	0.48	4.406	10.45	3.971	4.273	4.273
Larry528_260	17.15	4.421	7.11	4.735	0.73	4.453	10.43	4.003	4.319	4.311
Larry528_IF	17.15	4.392	7.11	4.704	0.48	4.413	10.43	3.977	4.280	4.280
Larry528_260	17.15	4.435	7.11	4.750	0.73	4.467	10.43	4.016	4.333	4.325
Joe79_260	19.48	4.68	1.25	4.738	0.61	4.709	9.90	4.258	4.338	4.330
Moe477	19.17	4.673	1.99	4.766	0.21	4.683	10.44	4.231	4.324	4.317
Ted16_260	20.21	4.725	−0.49	4.702	1.32	4.787	10.30	4.284	4.319	4.311
Curly394_IF	19.60	4.633	0.95	4.677	1.13	4.685	10.12	4.207	4.295	4.295
Curly394_260	19.60	4.654	0.95	4.698	1.51	4.724	10.12	4.226	4.331	4.323
Curly394_IF	19.60	4.643	0.95	4.687	1.13	4.696	10.12	4.216	4.305	4.305
Curly394_260	19.60	4.668	0.95	4.712	1.51	4.739	10.12	4.239	4.344	4.336
Momo_IF	19.66	4.660	0.81	4.698	1.00	4.707	10.28	4.226	4.302	4.302
Momo_260	19.66	4.660	0.81	4.698	1.40	4.725	10.28	4.226	4.319	4.311
Winnie_260	20.15	4.920	−0.35	4.903	−1.22	4.860	10.55	4.450	4.381	4.373
Howie_IF	19.54	4.675	1.10	4.726	1.45	4.743	10.30	4.317	4.347	4.347
Shemp319_280	21.31	4.663	−3.2	4.514	6.13	4.949	10.35	4.226	4.342	4.334
Shemp319_IF	21.31	4.870	−3.2	4.714	0.29	4.884	10.35	4.413	4.284	4.284
Shemp320_280	21.31	4.553	−3.2	4.407	7.41	4.890	10.46	4.122	4.286	4.278
Shemp320_IF	21.31	4.811	−3.2	4.657	0.76	4.847	10.48	4.355	4.248	4.248
Clotho_IF Clotho_280	19.66 19.66	4.243 4.317	0.81 0.81	4.277 4.352	0.15 -0.44	4.249 4.298	0.30 0.29	4.230 4.305	4.271 4.320	4.271 4.312
Average		4.583	1.98	4.669	1.20	4.638		4.192	4.317	4.313
standard deviation(%)		3.83	4.25	3.04	0.69	4.31		3.29	0.78	0.73
maximum range	−2.85 –	4.243 –	−3.2 –		−1.22 –		0.29 –	3.977 –	4.248 –	4.271 –
	1.31	4.920	7.11		7.41		10.45	4.450	4.387	4.379

[a]Except for Clotho, all instruments utilized Version 6 (Firmware 5.06) of the Proteome Lab XL-A/I data acquisition software. In the case of Clotho, Version 5.8 (Firmware 4.21) was used.